Article

Pd/Co$_3$O$_4$(111) Interface Formation

Maximilian Kastenmeier, Lukáš Fusek, Fatema Mohamed, Christian Schuschke, Michal Ronovský,
Tomáš Skála, Matteo Farnesi Camellone, Nataliya Tsud, Viktor Johánek, Stefano Fabris, Jörg Libuda,
Simone Piccinin, Yaroslava Lykhach,* Josef Mysliveček, and Olaf Brummel

ACCESS | Metrics & More | Article Recommendations | Supporting Information

ABSTRACT: The formation of the metal−oxide interface in the Pd/Co$_3$O$_4$(111) model catalyst was investigated by means of density functional theory (DFT), synchrotron radiation photoelectron spectroscopy (SRPES), and scanning tunneling microscopy (STM). The electronic metal−support interaction results in a substantial charge transfer at the interface yielding atomically dispersed Pd^{2+} species and partially oxidized Pd$^{\delta+}$ aggregates coupled with a partial reduction of Co$_3$O$_4$(111). Atomically dispersed Pd^{2+} species at the fcc site on the Co$_3$O$_4$(111) surface were found to be the most energetically favorable configuration. In comparison to the dispersed Pd^{2+} species, the formation of Pd dimers, trimers, and tetramers was found to be less favorable. The analysis of the Bader charges revealed a substantial net positive charge on Pd atoms in dimers, trimers, and tetramers which is consistent with the formation of partially oxidized Pd$^{\delta+}$ aggregates detected by SRPES. The analysis of the charge distribution in Co$_3$O$_4$(111) revealed a partial reduction of Co^{3+} to Co^{2+} cations in the first and second Co layers. According to DFT, Pd$^{\delta+}$ aggregates are prone to oxidation to PdO in the presence of O$_2$ and H$_2$O. The partially oxidized Pd$^{\delta+}$ and Pd$_4$O$_x$ aggregates form 1 to 2 monolayer thick clusters which serve as nuclei for the growth of metallic Pd^0 nanoparticles. At high Pd coverage, Pd nanoparticles coalesce resulting in the growth of two-dimensional islands that densely cover the Co$_3$O$_4$(111) substrate.
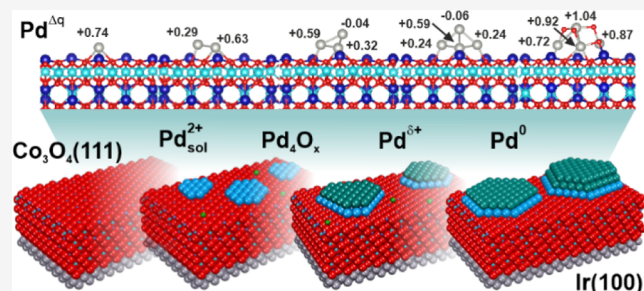
1. INTRODUCTION

Metal−oxide interfaces play a major role in the design of advanced functional materials for applications in catalysis, energy storage, and electronics.[1−5] Essentially, the factors controlling the formation of the metal−oxide interface involve the structural and thermodynamic parameters.[6] The corresponding arguments are particularly relevant for the growth and morphology of noble metal deposits on well-ordered oxides.[7−9] While the epitaxial relationship at the metal-oxide interface determines the crystallographic orientation of supported metal nanoparticles, the adhesion energy determines their morphology and stability. In particular, the adhesion energy between the supported metal particles and the oxide correlates strongly with the oxophilicity of the supported metal or the strength of metal−oxygen bonds at the interface.[10−12] More precisely, the adhesion energy increases with increasing heat of formation of the oxide of the supported metal or decreasing enthalpy of reduction of the oxide support to its next lower oxidation state. In this respect, metal−oxide interfaces between the oxophilic metals and reducible oxides endow the catalysts with high stability against sintering. From a chemical perspective, the interaction of supported metal nanoparticles with reducible oxides gives rise to complex phenomena that strongly impact their catalytic activity.[13−15] Among these, the electronic metal support interaction (EMSI)

is associated with the charge transfer at the metal−oxide interface, which leads to partial oxidation of the supported noble metal nanoparticles and partial reduction of the oxide support.[15−18] For instance, the EMSI yields a maximum partial charge around δ = +0.1e per Pt atom for Pt nanoparticles supported on reducible CeO$_2$(111) and Co$_3$O$_4$(111) substrates.[17,18] In the presence of specific anchoring sites, the charge transfer can be stronger and may yield atomically dispersed Pt^{2+} species.[19]

Generally, the assignment of the partially oxidized metallic clusters and ionic species by means of spectroscopic methods is challenging. Most often, the combination of initial state effects coupled with particle size effects and the charge transfer may result in considerable shifts of the spectral contributions rendering their binding energies similar to those typical for ionic species. Density functional theory (DFT) allows us to explore the structure, the charge transfer, and the affinity of
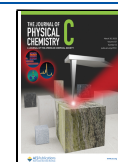
supported noble metal clusters to form stable oxide phases.[18−21] These parameters are particularly relevant at the nucleation stage of noble metal on reducible oxide substrates, when ultrasmall particles are particularly prone to oxidation.[21]

In the present paper, we investigate the formation of the interface between Pd nanoparticles and a well-ordered $Co_3O_4(111)$ substrate. The study was performed by means of DFT, synchrotron radiation photoelectron spectroscopy (SRPES), and scanning tunneling microscopy (STM). We found that the EMSI at the $Pd/Co_3O_4(111)$ interface involves a substantial charge transfer yielding atomically dispersed Pd^{2+} species and partially oxidized $Pd^{\delta+}$ aggregates in combination with Pd_4O_x clusters resulting in a partial reduction of the $Co_3O_4(111)$ substrate. At higher Pd coverage, metallic Pd nanoparticles grow in the form of two-dimensional islands with a strongly polarized interface.

2. METHODS

2.1. Computational Details. DFT calculations were performed using the Quantum ESPRESSO code[22,23] and employed a plane-wave basis set and ultrasoft pseudopotentials. The plane wave cutoff was set to 50 Ry for the wavefunctions and 500 Ry for the charge density. Occupations were smeared with a Gaussian broadening of 0.01 Ry. We employed the Perdew−Burke−Ernzerhof exchange and correlation functional and applied a Hubbard U correction of 3.0 eV to Co atoms, in agreement with our previous work on this system.[24] The $Co_3O_4(111)$ surfaces were modeled using a slab geometry with periodic replicas separated by vacuum in the direction normal to the surface in a (4×2) surface unit cell sampled at the Gamma point. Structural optimizations were performed with a convergence criterion for forces of 0.001 Ry/arb. units (0.025 eV/Å).

Adsorption energies of adatoms and small metallic Pd clusters supported on $Co_3O_4(111)$ were computed as $\frac{1}{N_{Pd}}(E_{slab/Pd} - (E_{slab} + N_{Pd}E_{Pd}))$, where $E_{slab/Pd}$ is the total energy of the $Co_3O_4(111)$ slab containing N_{Pd} atoms of Pd, E_{slab} is the total energy of the corresponding Pd-free $Co_3O_4(111)$ slab, and E_{Pd} is the total energy of a Pd atom in vacuum. The energy cost to create Pd_4O_x oxidized clusters supported on $Co_3O_4(111)$ surfaces has been computed considering three different sources for oxygen: O atoms from the surface, O atom from H_2O molecules, and O atoms from O_2 gas phase. When the source of O is the substrate, the formation energy of Pd_4O_x was computed as $(E_{slab/Pd_4O_x} + N_OE_{slab/red}) - (E_{slab/Pd_4} + N_{O_2}E_{slab})$, where E_{slab/Pd_4O_x} is the total energy of the slab containing the Pd_4O_x cluster, N_O is the number of O vacancies created on the surface in order to form the oxidized clusters, $E_{slab/red}$ is the total energy of the $Co_3O_4(111)$ surface with an O vacancy, E_{slab/Pd_4} is the total energy of the slab containing a Pd_4 metallic cluster, N_{O_2} is the number of O vacancies created on the substrate to form the cluster oxidized, and E_{slab} is the total energy of the stoichiometric surface. If the source of O is the H_2O molecule, the formation energies of supported clusters were computed as $(E_{slab/Pd_4O_x} + N_{H_2}E_{slab/H_2}) - (E_{slab/Pd_4} + N_{H_2O}E_{slab/H_2O})$, where N_{H_2} is the number of dissociated H_2 molecules adsorbed on the $Co_3O_4(111)$ surface after the dissociation of H_2O molecules and transfer of the resulting O atoms to the metallic

Pd_4 cluster to form the oxidized Pd_4O_x cluster, E_{slab/H_2} is the total energy of the $Co_3O_4(111)$ surface with H_2 atoms adsorbed, N_{H_2O} is the number of H_2O molecules adsorbed on the surface, and E_{slab/H_2O} is the total energy of the surface where N_{H_2O} are adsorbed. Finally, if the source of O_2 is the gas phase, we have computed the formation energy as $E_{slab/Pd_4O_x} - (E_{slab/Pd_4} - N_{O_2}E_{O_2})$, where E_{O_2} is the total energy of an O_2 molecule in gas phase.

2.2. Synchrotron Radiation Photoelectron Spectroscopy. High-resolution SRPES experiments were performed at the Materials Science Beamline (MSB), Elettra synchrotron light facility in Trieste, Italy. The MSB with a bending magnet source provided synchrotron light in the energy range of 21−1000 eV. The ultrahigh vacuum (UHV) end-station (base pressure 5×10^{-10} mbar) was equipped with a multichannel electron energy analyzer (Specs Phoibos 150), a rear view low-energy electron diffraction (LEED) optics, a sputter gun (Ar⁺), and a gas inlet system. Additionally, two electron-beam evaporators for the deposition of Co and Pd metals were installed.

The $Co_3O_4(111)$ film was prepared on Ir(100) following a multistep procedure.[25,26] First, the Ir(100) single crystal (MaTecK, 99.99%) was cleaned by Ar⁺ sputtering (300 K, 60 min), followed by annealing in an oxygen atmosphere (1×10^{-7} mbar, 3 min) and UHV (1 min) at 1325 K until no traces of carbon or any other contaminant were found in the photoelectron spectra. Subsequently, annealing of the Ir(100) crystal in an oxygen atmosphere (5×10^{-7} mbar, 1273 K, 5 min) yielded the $(2 \times 1)-O$ reconstruction. Then, an epitaxial $Co_3O_4(111)$ film was grown on the $(2 \times 1)-O/Ir(100)$ surface by physical vapor deposition (PVD) of Co metal (Goodfellow, 99.99%) in an oxygen atmosphere (2×10^{-6} mbar, Linde, 99.999%) at 273 K, followed by annealing in oxygen (1×10^{-6} mbar) at 523 K for 20 min and subsequent annealing in UHV at 680 K for 5 min. This preparation method yielded a continuous, stoichiometric $Co_3O_4(111)$ film with a thickness of 6.0 nm as determined from the attenuation of the Ir $4f_{7/2}$ intensity. The structure of the $Co_3O_4(111)$ film was verified by LEED. Earlier, the structure of the $Co_3O_4(111)$ film was investigated by means of STM and I−V LEED in great detail.[25,26] Briefly, the $Co_3O_4(111)$ film has a normal-spinel structure with a lattice parameter of 8.084 Å. The film contains Co^{3+} and Co^{2+} in octahedral and tetrahedral coordination, respectively. The lattice constant of the $Co_3O_4(111)$ film is 5.72 Å, as determined by LEED, which is similar to the value of bulk $Co_3O_4(111)$ (5.716 Å). The film is terminated by tetrahedrally coordinated Co^{2+} cations.

Pd (Goodfellow, 99.99%) was deposited by PVD from an electron-beam evaporator from a Pd rod (1.0 mm in diameter) onto the $Co_3O_4(111)$ film in a stepwise manner at 300 K in UHV. During the deposition, the voltage, the filament current, and the emission current were 1 kV, 5.0 A, and 3.0 mA, respectively. In order to maintain a stable deposition rate, the Pd evaporator was preheated for 5 min at deposition parameters with a closed shutter before each deposition step. The sample was grounded during the deposition. The nominal thickness of the Pd film was determined from the attenuation of the Co 2p intensity after the last deposition step and calibrated as a function of the deposition time. The Pd thickness is expressed in terms of monolayers (ML) considering 1 ML = 0.225 nm.
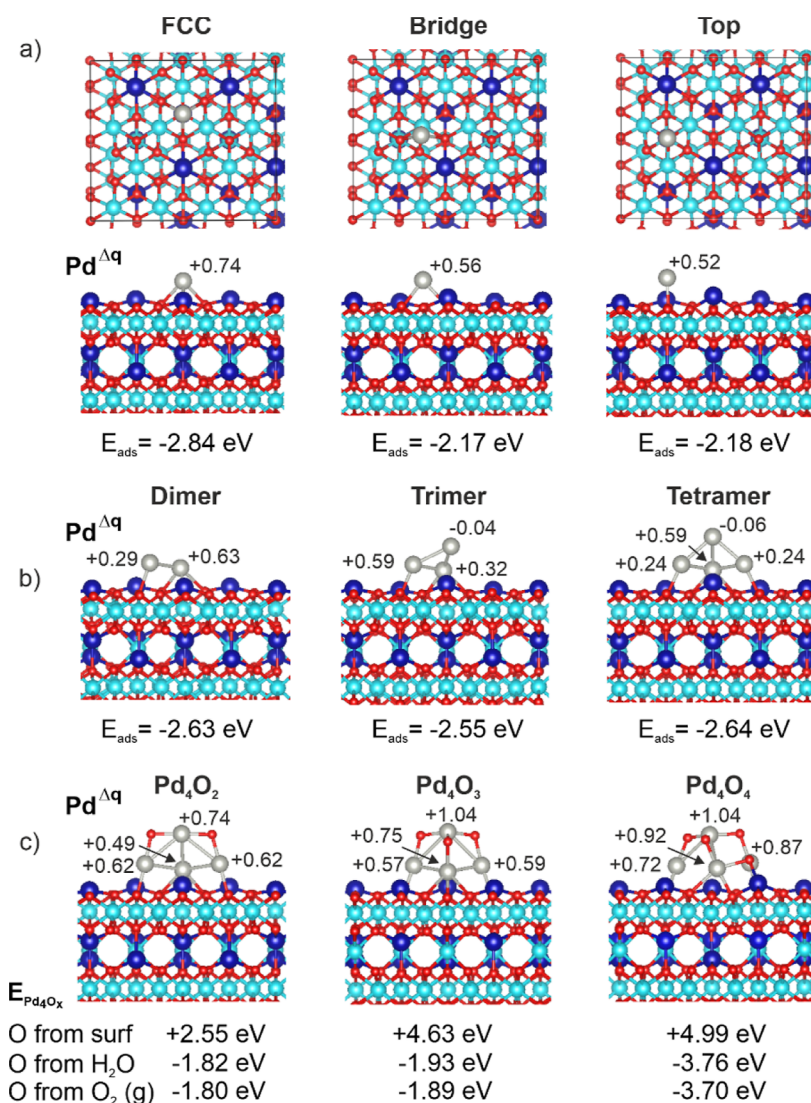
Figure 1. Top (a) and side (a−c) views of the optimized geometries of single Pd atoms (a), small Pd clusters (b), and Pd_4O_x clusters (c) on $Co_3O_4(111)$ according to DFT, where $x = 2$, 3, and 4. The Bader charge on the Pd atoms, Δq, is given in e. In the ball models, gray, red, blue, and turquoise balls represent Pd atoms and O^{2-}, Co^{2+}, and Co^{3+} ions, respectively.

The Pd 3d core level spectra were acquired with different photon energies between 410 and 810 eV. Additionally, the C 1s, O 1s, and Co 2p core level spectra were obtained with photon energies of 410, 650, and 930 eV, respectively. The binding energies in the spectra were calibrated with respect to the Fermi level. All spectra were acquired at constant pass energy and at an emission angle of the photoelectrons of 0° with respect to the sample normal. The total spectral resolutions were 200 meV ($h\nu$ = 60−180 eV), 350 meV ($h\nu$ = 410 eV), 500 meV ($h\nu$ = 550 eV), 650 meV ($h\nu$ = 650 eV), 850 meV ($h\nu$ = 810 eV), and 1 eV ($h\nu$ = 930 eV). All SRPES data were processed using KolXPD fitting software.[27] The spectral components in the Pd 3d spectra were fitted with an asymmetric Doniach-Šunjić function convoluted with a Gaussian profile after subtraction of Shirley background. During the experiments, the sample temperature was controlled by a DC power supply passing a current through Ta wires holding the sample. Temperature was monitored by a K-type thermocouple spot-welded to the back of the sample.

2.3. Scanning Tunneling Microscopy. The STM and X-ray photoelectron spectroscopy (XPS) experiments were performed in a UHV system (base pressure 1×10^{-10} mbar) at Charles University in Prague, Czech Republic. The chamber was equipped with a photoelectron spectrometer (Specs Phoibos 150), an Al Kα X-ray source, LEED, a home-built scanning tunneling microscope, and a quadrupole mass spectrometer (Pfeiffer PrismaPlus). The samples were heated radiatively.

Well-ordered $Co_3O_4(111)$ thin films were grown on a clean Ir(100) substrate (MaTecK). The clean Ir(100)−(5 × 1) surface was obtained by repeated cycles of ion sputtering and annealing at 1330 K. Afterwards, the (5 × 1) reconstruction was lifted by annealing at 1270 K in a background pressure of 5 × 10^{-7} mbar O$_2$ (Linde, 99.999%) yielding the Ir(100)−(2 × 1)−O structure. Co (Alfa Aesar, 99.995%) was deposited onto Ir(100)−(2 × 1)−O in a background O$_2$ atmosphere of 1.5 × 10^{-6} mbar at 300 K from an electron-heated Ta crucible. After Co deposition, the layer was further oxidized in 2 × 10^{-6} mbar of O$_2$ for 60 min at 600 K and finally at 680 K. To achieve the final $Co_3O_4(111)$ ordering, annealing in UHV at 720 K was performed. The layers were prepared with a nominal thickness of approximately 5.0 nm as determined by a quartz crystal
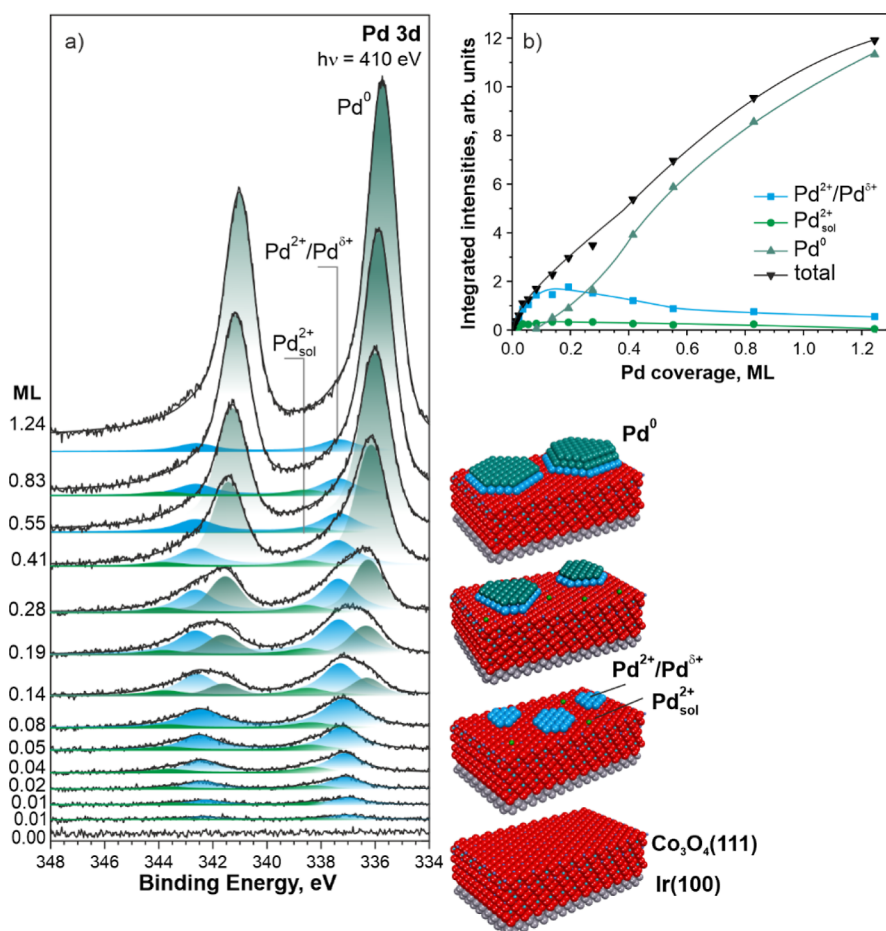
Figure 2. Pd 3d core level spectra (a) and the evolution of integrated Pd 3d intensities (b) as a function of Pd coverage. The Pd 3d spectra were acquired with a photon energy of 410 eV. In the ball models, green, cyan, and jade balls represent atomically dispersed Pd^{2+} species, $Pd^{\delta+}$ aggregates, and Pd^0 particles, respectively, while red, blue, and turquoise balls represent O^{2-}, Co^{2+}, and Co^{3+} ions in the $Co_3O_4(111)$ film, and gray balls represent Ir in the Ir(100) substrate.

microbalance (QCM) and by attenuation of the Ir 4f XPS signal. The $Pd/Co_3O_4(111)$ model catalysts were prepared by deposition of Pd on the as-prepared $Co_3O_4(111)$ film. Pd deposition was performed from electron-heated Pd wire (Goodfellow, 99.99%) in UHV at 300 K. The thickness of the deposited Pd film was determined by means of XPS and QCM.

STM imaging was performed at 300 K using electrochemically etched W tips. STM images were obtained at tunneling voltages and tunneling currents as follows: $Co_3O_4(111)$ at −2.5 V, 0.15 nA; and as-prepared $Pd/Co_3O_4(111)$ at −2.0 V, 0.35 nA.

3. RESULTS AND DISCUSSION

3.1. Single Pd Atoms and Pd Clusters on $Co_3O_4(111)$: DFT Study.
First, we investigated the adsorption of single Pd atoms and small Pd clusters on the $Co_3O_4(111)$ substrate by means of DFT. The optimized geometries of the model $Pd/Co_3O_4(111)$ systems are summarized in Figure 1a,b. Three adsorption sites were considered for single Pd atoms denoted as fcc, bridge, and top sites in Figure 1a. Among these, the most favorable fcc site yields the adsorption energy of −2.84 eV. The bridge and top sites are less favorable with the adsorption energies of −2.17 and −2.18 eV, respectively. The calculated Bader charges, Δq, on Pd atoms adsorbed at fcc, bridge, and top sites are $+0.74e$, $+0.56e$, and $+0.52e$,

respectively. Interestingly, for the Pd dimer, the adsorption energy per Pd atom is −2.63 eV, which is lower than that calculated for a single Pd atom at fcc site. The adsorption energy slightly decreases for a trimer and increases for a tetramer. The evolution of the Bader charges on Pd atoms in the Pd clusters reveals a strong charge transfer from the Pd atoms which form the shortest bonds with the $Co_3O_4(111)$ surface, while those with longer bonds exhibit a smaller positive charge or even negative charge (see Figure 1b). However, the net charge on small Pd clusters is positive and suggests the formation of partially oxidized $Pd^{\delta+}$ aggregates. Nevertheless, we found that the average charge per Pd atom in $Pd^{\delta+}$ aggregates shows a tendency to decrease with increasing size of the aggregates.

Next, we computed the distribution of the charge transferred from the Pd tetramer within the $Co_3O_4(111)$ substrate (see Supporting Information, Section S1). We found that the charge is largely delocalized over cobalt and oxygen ions in the top two cobalt and top two oxygen layers. The comparison of the adsorption energies calculated for single Pd atoms and Pd clusters suggests that the $Pd-Co_3O_4(111)$ interaction is stronger than $Pd-Pd$ interaction resulting in a rather weak thermodynamic driving force for Pd atoms to coalesce into particles.

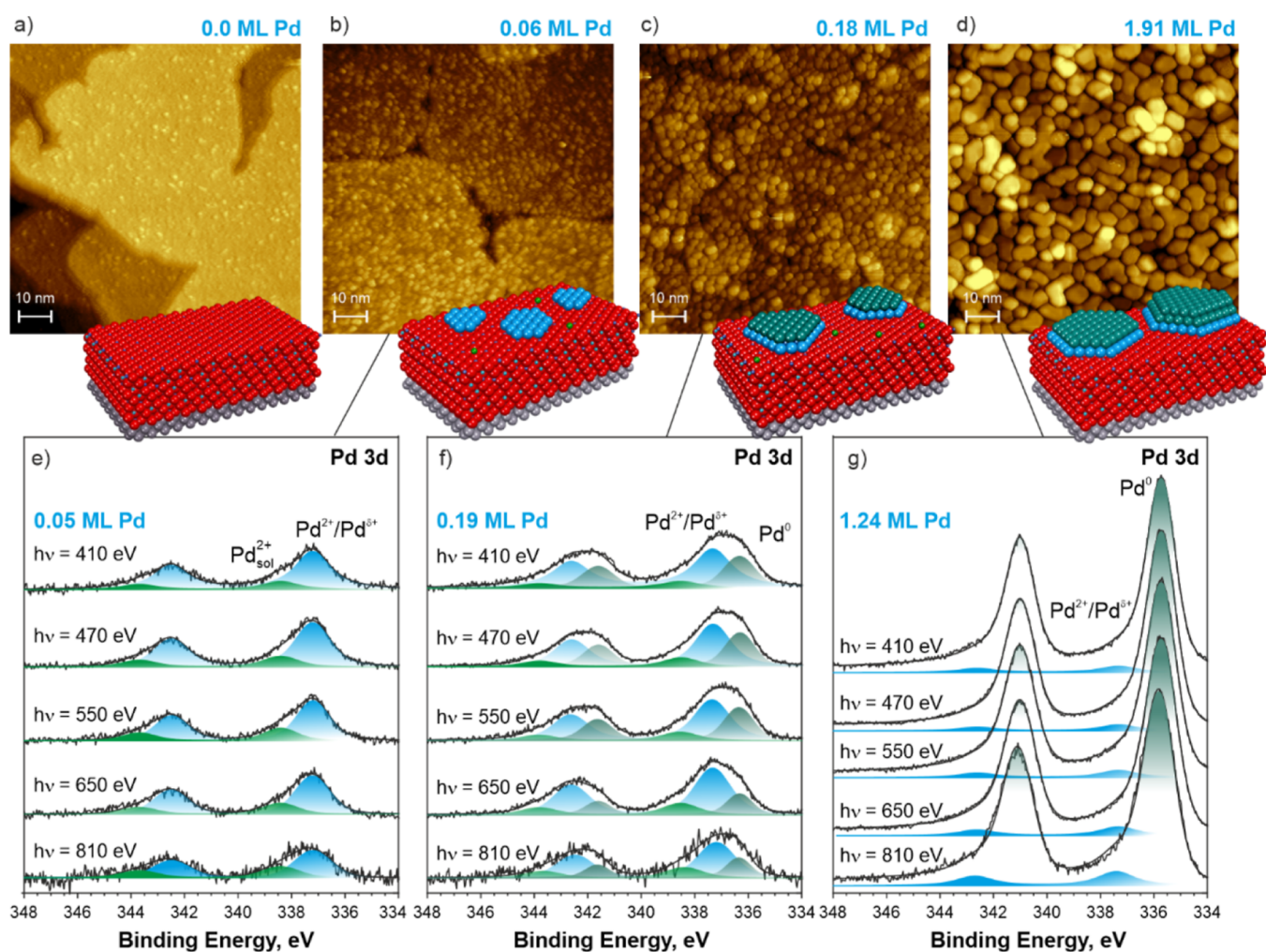Additionally, we have investigated the formation of Pd_4O_x clusters on $Co_3O_4(111)$, namely, Pd_4O_2, Pd_4O_3, and Pd_4O_4,

Figure 3. STM images (a−d) and Pd 3d spectra (e−g) obtained from the $Co_3O_4(111)$ (a) and $Pd/Co_3O_4(111)$ (b−g) model catalysts. The Pd 3d spectra were acquired with photon energies between 410 and 810 eV.

starting from a Pd tetramer and adding two, three, and four O atoms. The optimized geometries of the supported Pd_4O_2, Pd_4O_3, and Pd_4O_4 clusters are shown in Figure 1c. When O atoms are taken from the $Co_3O_4(111)$ surface, the energy costs to create the Pd_4O_2, Pd_4O_3, and Pd_4O_4 clusters are +2.55, +4.63, and +4.99 eV, respectively. This is due to the high energy cost required to create O vacancies in the $Co_3O_4(111)$ support. If the source of oxygen is H_2O molecules, the gains in energy to form the Pd_4O_2, Pd_4O_3, and Pd_4O_4 clusters are −1.82, −1.93, and −3.76 eV, respectively. After the reaction, H atoms are adsorbed on the $Co_3O_4(111)$ surface. The adsorption energy of each H_2 molecule after dissociation on the $Co_3O_4(111)$ surface is found to be −3.33 eV. In contrast, under the assumption that the H atoms desorb as H_2, the energy costs for the formation of Pd_4O_2, Pd_4O_3, and Pd_4O_4 clusters are +4.82, +8.04, and +9.54 eV, respectively.

When, instead, the source of oxygen is O_2 molecules from a gas phase, the gains in energy to form the Pd_4O_2, Pd_4O_3, and Pd_4O_4 clusters are −1.80, −1.89, and −3.70 eV, respectively. This behavior suggests strong tendency for small Pd clusters to get oxidized to PdO in the presence of an oxygen source. With respect to the oxidation state of Pd atoms in the Pd_4O_x clusters, we refer to the computed Δq charges on Pd atoms in Pd_2O, PdO, and PdO_2 compounds which are $+0.44e$ (Pd^{1+}), $+0.86e$ (Pd^{2+}), and $+1.47e$ (Pd^{4+}), respectively. Accordingly,

we suggest that the oxidation state of the Pd atoms in the Pd_4O_x clusters varies between +1 and +2.

3.2. Identification of Pd Species on $Co_3O_4(111)$ by Means of SRPES. The Pd 3d spectra obtained during the stepwise deposition of Pd onto the well-ordered $Co_3O_4(111)$ film are plotted in Figure 2a. In the limit of small Pd coverage, two doublet peaks emerge at 337.1 eV ($3d_{5/2}$) and 338.4 eV ($3d_{5/2}$). In line with the DFT studies discussed above, the corresponding contributions can be assigned to the small $Pd^{\delta+}$ aggregates and atomically dispersed Pd^{2+} species supported on $Co_3O_4(111)$, respectively. However, we cannot completely rule out that the fraction of atomically dispersed Pd species emerges due to implantation of Pd ions emitted from the electron-beam evaporator during Pd deposition. The assignment of the atomically dispersed Pd^{2+} species is consistent with the binding energy of Pd^{2+} ions anchored onto CeO_2 surfaces and those in the $Pd-CeO_2$ solid solution.[28−30] Thus, we label the corresponding spectral contribution arising from a solid solution of Pd^{2+} ions in $Co_3O_4(111)$ as Pd_{sol}^{2+} in Figure 2a.

The binding energy of the Pd $3d_{5/2}$ contribution associated with the small $Pd^{\delta+}$ aggregates is about 2.0 eV higher with respect to that of the metallic Pd^0 state (334.9−335.2 eV).[31−33] However, in the case of supported metal nanoparticles, substantial core level shifts may result from a combination of structural and electronic effects both in the

initial and in the final state.[34,35] For instance, Wang et al.[34] reported an increase of the Pd 3d binding energy by as much as 1.3 eV with decreasing size of Pd nanoparticles supported on Al_2O_3 from 19.1 to 2.1 nm. In the presence of EMSI, the shift of the core-level binding energy may further increase depending on the direction and the magnitude of the charge transfer at the metal/oxide interface.[18] In fact, the net positive charge of supported $Pd^{\delta+}$ aggregates predicted by DFT (Section 3.1) is largely consistent with the shift of Pd 3d core level to higher binding energy. It should be noted that adsorption of CO has strong influence on the binding energy of Pd 3d core level.[36,37] Although we observed gradual accumulation of carbonaceous species, we rule out adsorption of CO at small Pd coverages where contribution from the $Pd^{\delta+}$ aggregates dominates (see Supporting Information, Section S2, Figure S1). It is noteworthy that the binding energy of the corresponding $Pd^{\delta+}$ contribution does not change as a function of Pd coverage. This observation suggests that the $Pd^{\delta+}$ aggregates contain less than ~30 atoms for which the binding energy of the Pd 3d core level virtually does not depend on the particle size.[38] Alternatively, the same $Pd\ 3d_{5/2}$ contribution could be assigned to Pd_4O_x clusters since its binding energy matches that associated with the Pd^{2+} state in PdO.[31,32] Note that ultrasmall $Pd^{\delta+}$ aggregates are particularly prone to oxidation by O_2 and water, as discussed in Section 3.1. It should be noted that traces of O_2 and water are omnipresent in the residual atmosphere of a UHV chamber. Since the $Pd^{\delta+}$ aggregates and Pd_4O_x clusters cannot be reliably resolved based on their binding energy, we label the corresponding peak as a joint $Pd^{2+}/Pd^{\delta+}$ contribution in Figure 2a.

At higher Pd coverages, a new doublet peak emerges at 336.2 eV $(3d_{5/2})$ and grows rapidly while shifting to lower binding energies. Initially, the binding energy shift of this contribution with respect to the bulk Pd^0 is 1.0 eV and decreases to 0.4 eV by approaching the binding energy of 335.7 eV $(3d_{5/2})$ at a Pd coverage of 1.24 ML. The observed behavior is consistent with the growth of metallic Pd^0 nanoparticles. Based on the evolution of the integrated Pd 3d intensities in Figure 2b, the ionic Pd_{sol}^{2+} species and $Pd^{\delta+}/Pd_4O_x$ clusters serve as nuclei for the growth of the metallic nanoparticles. In particular, the decrease of the joint $Pd^{2+}/Pd^{\delta+}$ contribution coincides with the emergence of the metallic Pd^0 contribution at Pd coverages above 0.1 ML (Figure 2b). This behavior is qualitatively similar to the growth of Pt nanoparticles on the $Co_3O_4(111)$ film.[17,39]

3.3. Morphology of the Pd/Co₃O₄(111) Model Catalyst.
STM images obtained from the well-ordered $Co_3O_4(111)/Ir(100)$ and $Pd/Co_3O_4(111)/Ir(100)$ model catalysts are shown in Figure 3a–d.

The morphology of the $Co_3O_4(111)$ films has been investigated earlier.[40] Briefly, the $Co_3O_4(111)$ film represents a continuous layer terminated by atomically flat $Co_3O_4(111)$ islands with an average step height of approximately 0.45 nm. The lateral size of the terminating islands varies between 10 and 100 nm. The Pd nanoparticles grow in the form of clusters homogeneously dispersed onto the surface of $Co_3O_4(111)$. Since the apparent size of the supported nanoparticles in the STM is affected by tip-convolution effects,[41] we estimated the nanoparticle sizes based on the particle density determined by STM and the amount of deposited metal per unit area as determined by QCM. For estimating the particle size, we assume a cylindrical particle shape, which appears to be the best approximation based on the height profile of Pd

nanoparticles as obtained with STM (see Figure S2, Supporting Information). The structural parameters of Pd deposit determined for three Pd coverages are listed in Table 1.

Table 1. Structural Parameters of the Model Pd/Co₃O₄(111) Catalysts

			assumption of cylindrical shape		
Pd (ML)	atoms per cluster	cluster density (cm^{-2})	number of ML	average diameter (nm)	surface coverage (%)
0.06	15	0.7×10^{13}	1	1.1	7
0.18	34	0.8×10^{13}	2	1.3	11
1.91	1084	0.27×10^{13}	3–4	5–6	60–70

The particle sizes were estimated assuming the particle heights between 1 and 4 ML. In agreement with the height profile analysis (Figure S2, Supporting Information), we assume that the heights of the Pd clusters correspond to 1 ML (for 0.06 ML Pd), 2 ML (for 0.18 ML Pd), and 3–4 ML (for 1.91 ML Pd) similar to our previous analysis of the Pd/$Co_3O_4(111)$ model catalysts.[42] Thus, for a Pd coverage of 0.06 ML, the resulting diameter of the $Pd^{\delta+}$ clusters is about 1.1 nm (cylindrical shape) which corresponds to 15 Pd atoms per cluster. In the case of 0.18 ML Pd coverage, the Pd nanoparticles contain about 34 Pd atoms per particle. The corresponding size of the Pd nanoparticles is 1.3 nm. At 1.91 ML Pd coverage, we observed sintering of Pd nanoparticles yielding flat faceted islands which densely cover the $Co_3O_4(111)$ surface. The estimated heights of the Pd nanoparticles in the STM image are between 3 and 4 ML.

For the three Pd coverages similar to those investigated by means of STM, we performed a depth profiling of the oxidation state of the Pd species using photon energies between 410 eV and 810 eV. The corresponding Pd 3d spectra obtained from the Pd/$Co_3O_4(111)$ model catalysts are shown in Figure 3e–g. The intensity ratios between the spectral contributions from the Pd_{sol}^{2+}, the joint $Pd^{2+}/Pd^{\delta+}$, and the Pd^0 are plotted in Figure S3 as a function of photon energy (see the Supporting Information). The corresponding inelastic mean free paths of photoelectrons,[43] λ, are given in Table S5 (see the Supporting Information). The evolution of the intensity ratios as a function of photon energy suggests that Pd_{sol}^{2+} is distributed subsurface with respect to the $Pd^{2+}/Pd^{\delta+}$ species. However, at high Pd coverages, the $Pd^{2+}/Pd^{\delta+}$ species get buried below the metallic Pd^0 nanoparticles. Thus, the Pd/$Co_3O_4(111)$ interface region is formed by oxidized Pd_{sol}^{2+} species and partially oxidized $Pd^{2+}/Pd^{\delta+}$ aggregates resulting from the charge transfer at the Pd/$Co_3O_4(111)$ interface.

3.4. Charge Transfer at the Pd/Co₃O₄(111) Interface.
Generally, the charge transfer at the Pd/$Co_3O_4(111)$ interface results in the reduction of the Co^{3+} ions to Co^{2+} and can be estimated by means of different methods.[18,24] Among these, the most accurate method involves the evaluation of the Co^{3+}/Co^{2+} concentration ratio based on the intensities of the corresponding Co^{3+} and Co^{2+} features in the valence-band spectra of $Co_3O_4(111)$.[24] The basics of the quantitative approach using resonant photoemission spectroscopy (RPES) method are demonstrated in Figure 4a. Here, the Co^{3+}/Co^{2+} concentration ratio is proportional to the intensity ratio of the resonantly enhanced valence-band features associated with Co^{3+} and Co^{2+} ions.[24] Alternatively, the Co^{3+}/Co^{2+} concentration ratio can be determined directly from the intensities of

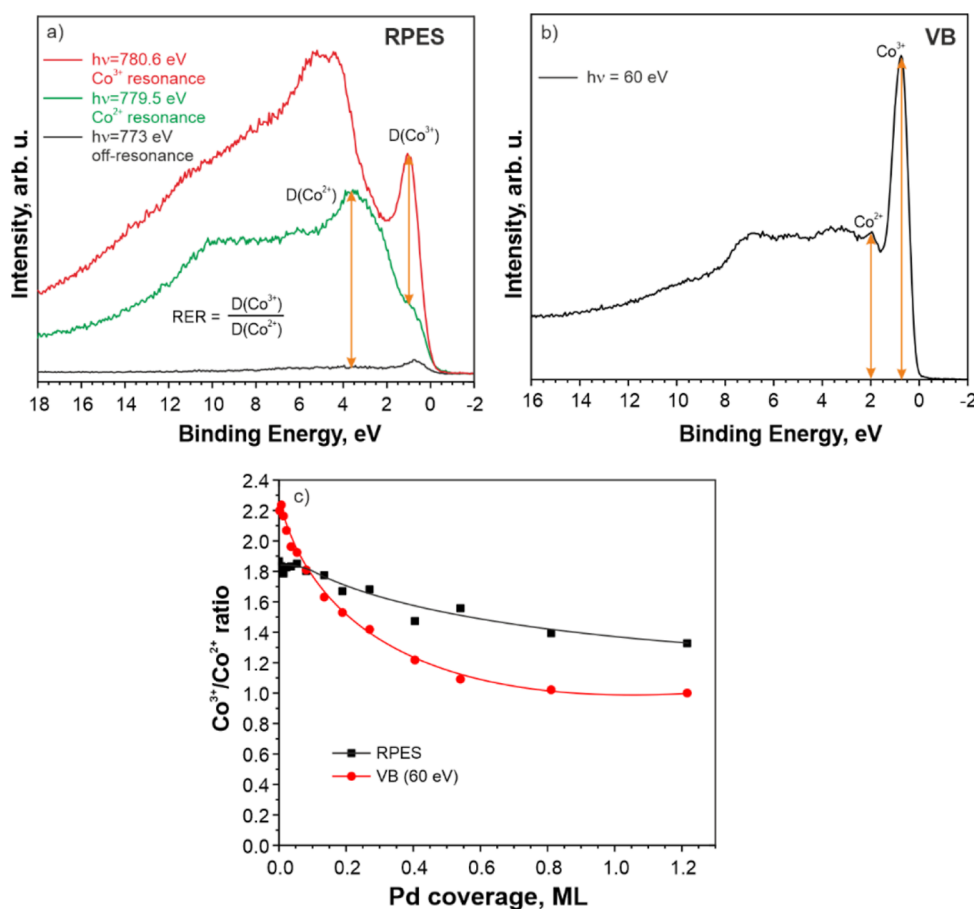**Figure 4.** (a) Set of three valence-band spectra obtained from the $Co_3O_4(111)$ film at photon energies of 780.6, 779.5, and 773.0 eV corresponding to the resonant photoemission in Co^{3+} and Co^{2+} cations and off-resonance condition, respectively and (b) valence-band spectrum obtained from the $Co_3O_4(111)$ film with a photon energy of 60 eV. (c) Evolution of the Co^{3+}/Co^{2+} concentration ratio as a function of Pd coverage determined based on RPES (black squares) and valence-band spectra obtained with a photon energy of 60 eV (red circles).

the corresponding Co^{3+} and Co^{2+} features in the valence-band spectra[24] obtained with high surface sensitivity (Figure 4b). The evolution of the Co^{3+}/Co^{2+} concentration ratios obtained by both methods is plotted as a function of the Pd coverage in Figure 4c. We found that the Co^{3+}/Co^{2+} concentration ratio determined from the valence-band spectra obtained with a photon energy of 60 eV decreases sharply as a function of Pd coverage until it reaches 1.0 at 1.24 ML Pd coverage. In contrast, the decrease of the Co^{3+}/Co^{2+} concentration ratio obtained by SRPES is less pronounced. The observed differences in the Co^{3+}/Co^{2+} concentration ratios determined by the two methods are related to the different information depths accessed using different photon energies. The specific differences in the information depths between the two methods can be employed for the depth profiling of the charge distribution across the $Co_3O_4(111)$ film thickness as a function of Pd coverage.

Generally, the number of electrons transferred from the Pd deposit to the $Co_3O_4(111)$ film corresponds to the number of the Co^{3+} ions reduced to Co^{2+}. We simulated the Co^{3+}/Co^{2+} concentration ratios assuming different distribution profiles of the Co^{3+} and Co^{2+} ions within the Co layers of the $Co_3O_4(111)$ structure.[25,26]

We assume that the majority of the signal ($\sim$95%) originates from the information depth corresponding to $3 \times \lambda$. The simulated Co^{3+}/Co^{2+} concentration ratios were fitted to match the Co^{3+}/Co^{2+} concentration ratios obtained by both RPES

and VB, as shown in Figure 4c. The best fitting results were obtained assuming the depth distribution of the Co^{3+} and Co^{2+} ions plotted in Figure 5. We found that the charge transfer involves the top two Co layers. This observation is in qualitative agreement with the DFT calculations regarding the direction of the charge transfer and its depth distribution despite the limitations of the DFT model associated with the localization of the charge (see Supporting Information, Section S1). In the ideal $Co_3O_4(111)$ structure (see Figure 5c), the first layer contains Co^{2+} and the second contains Co^{3+} ions. However, prior to Pd deposition, we found that the first Co layer contains a small amount of Co^{3+} probably at the defect sites. These surface Co^{3+} cations are preferentially reduced to Co^{2+} at the early stages of Pd growth. Then, the Co^{3+} cations in the second layer start to get reduced. At 1.24 ML Pd coverage, as much as 50% of Co^{3+} cations in the second layer are reduced to Co^{2+}. The total number of electrons transferred from Pd nanoparticles to the $Co_3O_4(111)$ film is plotted in Figure 5d as a function of Pd coverage.

Considering the number of Pd atoms per particle and the corresponding number of electrons transferred to the $Co_3O_4(111)$ film, we estimated the charge δ transferred per Pd atom for Pd coverages listed in Table 1. Thus, we obtained δ of +1.02, +0.93, and +0.21 for Pd coverages of 0.06 ML, 0.18 ML, and 1.91 Pd, respectively. This observation suggests that the charge transfer is located at the interface and decreases with increasing height of Pd nanoparticles. Interestingly, the
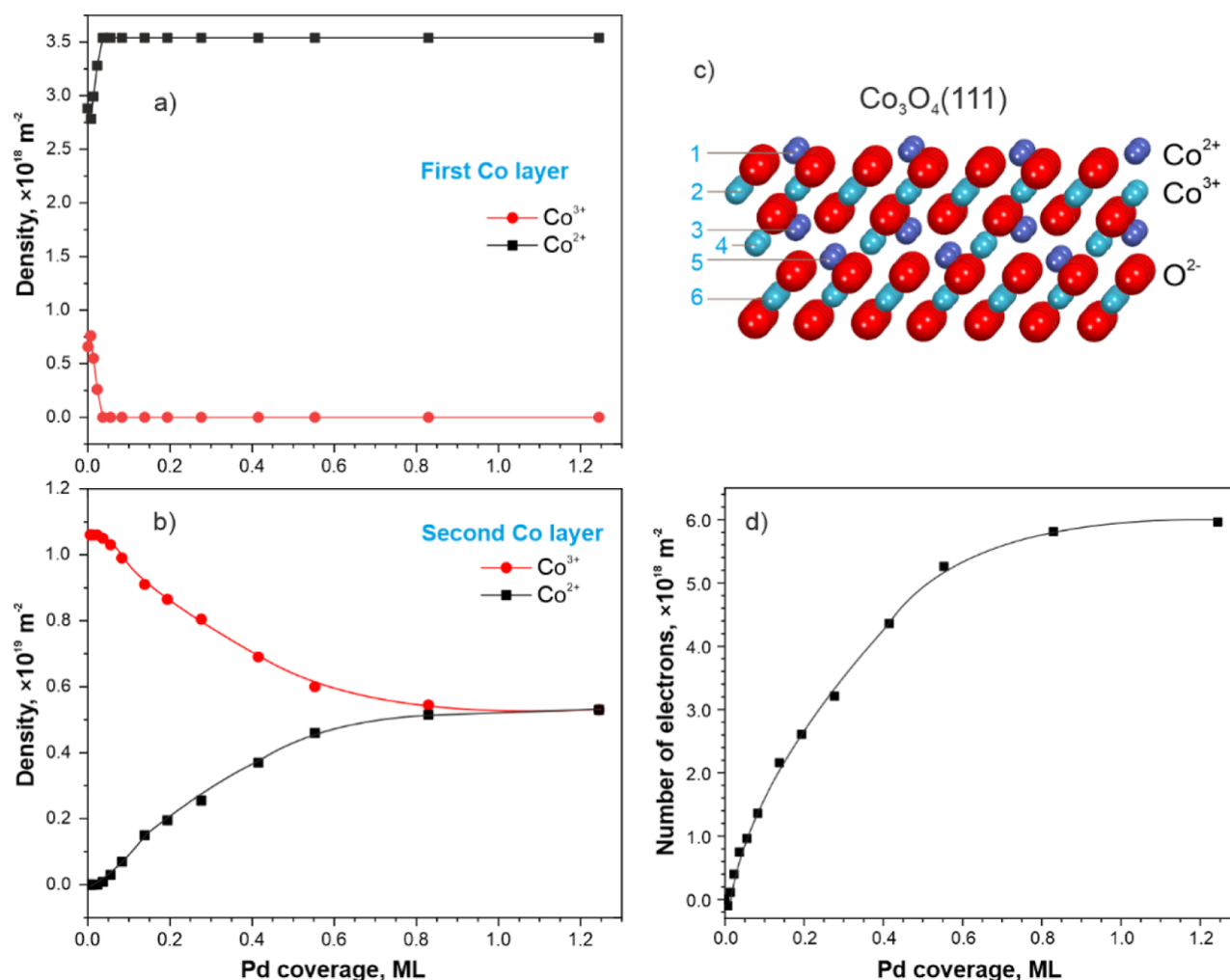
Figure 5. Distribution of Co^{3+} (red circles) and Co^{2+} (black squares) cations in the first (a) and second (b) Co layers of the $Co_3O_4(111)$ film as a function of Pd coverage. The ball model in (c) represents the structure of the $Co_3O_4(111)$ film. Red, blue, and turquoise balls represent O^{2-}, Co^{2+}, and Co^{3+} ions, respectively. The total number of electrons transferred at the $Pd/Co_3O_4(111)$ interface as a function of the Pd coverage (d).

analysis of the intensity ratio between metallic Pd^0 and the joint $Pd^{2+}/Pd^{\delta+}$ contributions as a function of photon energy suggests that in 3 ML thick Pd nanoparticles, only 50% (i.e., 0.5 ML) of Pd atoms in the interface layer are partially oxidized, while the remaining 2.5 ML are metallic (see Supporting Information, Section S4).

Still, the charge of $\delta = +1.02e$ per Pd atom at small Pd coverage (0.06 ML) is substantially higher than the corresponding maximum δ charge per Pt atom ($\delta = +0.11e$).[17,18] Noteworthy, the differences in the magnitude of the charge transfer correlate inversely with the reduction potentials of Pd and Pt metals.[44]

We assume that the oxidation of $Pd^{\delta+}$ aggregates by lattice oxygen of $Co_3O_4(111)$ could lead to the strong reduction of $Co_3O_4(111)$. However, this process is estimated to be highly endothermic by DFT (see Section 3.1). We may still speculate that the oxidation of $Pd^{\delta+}$ aggregates to Pd_4O_x could occur at defect sites where the energy of vacancy formation is lower than the one at the terrace sites.

It should be noted that $Pd^{\delta+}$ aggregates are prone to oxidation to Pd_4O_x in the presence of O_2 and H_2O. Our DFT calculations suggest that the oxidation of the Pd tetramer results in a charge transfer to oxygen atoms in the Pd_4O_4 cluster and to the $Co_3O_4(111)$ support ($0.79e$) (see

Supporting Information, Section S5). In $Co_3O_4(111)$, the charge is delocalized mostly over the top two Co layers ($0.44e$) and the top two O layers ($0.40e$), similar to the case of the metallic Pt_4 cluster (see Supporting Information, Section S1). Thus, DFT calculations suggest a strong tendency for the charge transfer to the Co_3O_4 support regardless of the degree of the oxidation of the Pd cluster.

Among other possible causes for the pronounced charge transfer at the $Pd/Co_3O_4(111)$ interface, we considered a band bending effect and, particularly, the influence of adventitious carbon deposits (see Supporting Information, Section S2). Our estimations suggest that the band bending effect, both in the presence and in the absence of adventitious carbon, has no significant impact on the magnitude of the observed charge transfer. Specifically, the contribution of the band banding to the charge transfer at 0.06 ML Pd coverage is less than 2%.

■ CONCLUSIONS

The formation of the $Pd/Co_3O_4(111)$ interface was investigated by means of DFT, SRPES, and STM. We found that the interaction of Pd with $Co_3O_4(111)$ is accompanied by a substantial charge transfer yielding atomically dispersed Pd^{2+} species and partially oxidized $Pd^{\delta+}$ aggregates in combination

with Pd_4O_x clusters. The formation of these species is accompanied by a partial reduction of $Co_3O_4(111)$.

DFT predicted preferential adsorption of Pd atoms at fcc sites, while adsorption at top and bridge sites on the $Co_3O_4(111)$ surface was found to be energetically less favorable. With respect to the formation of small Pd clusters, the adsorption energy of Pd atoms in the form of dimers, trimers, and tetramers was found to be lower than the adsorption energy of a single Pd atom at an fcc site. The distribution of Bader charges on Pd atoms in dimers, trimers, and tetramers indicated a substantial positive charge on those atoms that form short bonds with $Co_3O_4(111)$. The transferred charge is delocalized over the top two Co and top two O layers of the $Co_3O_4(111)$ slab. However, complete oxidation of the partially oxidized $Pd^{\delta+}$ tetramer with lattice oxygen from $Co_3O_4(111)$ was found unfavorable. In contrast, the oxidation of the $Pd^{\delta+}$ tetramer to Pd_4O_4 with O_2 and H_2O is favorable. This process is accompanied by a charge transfer from the Pd atoms to oxygen atoms in Pd_4O_4 and $Co_3O_4(111)$. In the $Co_3O_4(111)$ slab, the transferred charge is delocalized over top two Co and top two O layers.

The atomically dispersed Pd^{2+} species and $Pd^{\delta+}/Pd_4O_x$ clusters were identified spectroscopically and characterized with respect to their depth distribution and morphology. Specifically, partially oxidized $Pd^{\delta+}$ aggregates and Pd_4O_x clusters were found to exist in the form of 1 to 2 ML thick clusters. The metallic Pd^0 nanoparticles grow on top of these clusters. The charge transferred from oxidized Pd^{2+} and partially oxidized $Pd^{\delta+}$ species leads to the reduction of Co^{3+} ions to Co^{2+} in the first and the second Co layer. At high Pd coverage, two-dimensional clusters coalesce yielding flat faceted islands which densely cover $Co_3O_4(111)$.

Our study shows that the magnitude of the EMSI determines the morphology of supported Pd nanoparticles on reducible oxides. The effect can be employed to tune the reactivity and selectivity of the catalyst, for example, by controlling the oxidation state, the partial charge, and the fraction of low-coordinated sites in supported noble metal nanoparticles.

■ ASSOCIATED CONTENT

⬛ Supporting Information

The Supporting Information is available free of charge at https://pubs.acs.org/doi/10.1021/acs.jpcc.3c00261.

    DFT calculations of the charge distribution and SRPES and STM data analyses (PDF)

■ AUTHOR INFORMATION

Corresponding Author

    Yaroslava Lykhach − *Interface Research and Catalysis, ECRC, Friedrich-Alexander-Universität Erlangen-Nürnberg, 91058 Erlangen, Germany;* ⦿ orcid.org/0000-0003-3989-0365; Email: yaroslava.lykhach@fau.de

Authors

    Maximilian Kastenmeier − *Interface Research and Catalysis, ECRC, Friedrich-Alexander-Universität Erlangen-Nürnberg, 91058 Erlangen, Germany;* ⦿ orcid.org/0000-0002-4532-8072

    Lukáš Fusek − *Interface Research and Catalysis, ECRC, Friedrich-Alexander-Universität Erlangen-Nürnberg, 91058 Erlangen, Germany; Faculty of Mathematics and Physics,*

Department of Surface and Plasma Science, Charles University, 18000 Prague, Czech Republic; ⦿ orcid.org/0000-0002-2189-4731

    Fatema Mohamed − *Faculty of Science, Department of Physics, University of Khartoum, 11115 Khartoum, Sudan*

    Christian Schuschke − *Interface Research and Catalysis, ECRC, Friedrich-Alexander-Universität Erlangen-Nürnberg, 91058 Erlangen, Germany;* ⦿ orcid.org/0000-0002-5635-1112

    Michal Ronovský − *Faculty of Mathematics and Physics, Department of Surface and Plasma Science, Charles University, 18000 Prague, Czech Republic; Present Address: European Synchrotron Radiation Facility, 38043 Grenoble, France*

    Tomáš Skála − *Faculty of Mathematics and Physics, Department of Surface and Plasma Science, Charles University, 18000 Prague, Czech Republic;* ⦿ orcid.org/0000-0003-2909-9422

    Matteo Farnesi Camellone − *Consiglio Nazionale delle Ricerche-Istituto Officina dei Materiali (CNR-IOM), 34136 Trieste, Italy;* ⦿ orcid.org/0000-0001-9180-0115

    Nataliya Tsud − *Faculty of Mathematics and Physics, Department of Surface and Plasma Science, Charles University, 18000 Prague, Czech Republic;* ⦿ orcid.org/0000-0001-7439-7731

    Viktor Johánek − *Faculty of Mathematics and Physics, Department of Surface and Plasma Science, Charles University, 18000 Prague, Czech Republic;* ⦿ orcid.org/0000-0002-8833-5870

    Stefano Fabris − *Consiglio Nazionale delle Ricerche-Istituto Officina dei Materiali (CNR-IOM), 34136 Trieste, Italy*

    Jörg Libuda − *Interface Research and Catalysis, ECRC, Friedrich-Alexander-Universität Erlangen-Nürnberg, 91058 Erlangen, Germany;* ⦿ orcid.org/0000-0003-4713-5941

    Simone Piccinin − *Consiglio Nazionale delle Ricerche-Istituto Officina dei Materiali (CNR-IOM), 34136 Trieste, Italy;* ⦿ orcid.org/0000-0002-3601-7141

    Josef Mysliveček − *Faculty of Mathematics and Physics, Department of Surface and Plasma Science, Charles University, 18000 Prague, Czech Republic;* ⦿ orcid.org/0000-0003-2305-2711

    Olaf Brummel − *Interface Research and Catalysis, ECRC, Friedrich-Alexander-Universität Erlangen-Nürnberg, 91058 Erlangen, Germany;* ⦿ orcid.org/0000-0001-5968-0774

Complete contact information is available at:
https://pubs.acs.org/10.1021/acs.jpcc.3c00261

Author Contributions

M.K. and L.F. contributed equally. M.K. and L.F. are first authors. The manuscript was written through contributions of all authors. All authors have given approval to the final version of the manuscript.

Notes

The authors declare no competing financial interest.

■ REFERENCES

(1) van Deelen, T. W.; Hernández Mejía, C.; de Jong, K. P. Control of Metal-Support Interactions in Heterogeneous Catalysts to Enhance Activity and Selectivity. *Nat. Catal.* **2019**, *2*, 955−970.

(2) Zou, S.; Lou, B.; Yang, K.; Yuan, W.; Zhu, C.; Zhu, Y.; Du, Y.; Lu, L.; Liu, J.; Huang, W.; et al. Grafting Nanometer Metal/Oxide Interface Towards Enhanced Low-Temperature Acetylene Semi-Hydrogenation. *Nat. Commun.* **2021**, *12*, 5770.

(3) Kim, J.; Choi, H.; Kim, D.; Park, J. Y. Operando Surface Studies on Metal-Oxide Interfaces of Bimetal and Mixed Catalysts. *ACS Catal.* **2021**, *11*, 8645−8677.

(4) Suchorski, Y.; Kozlov, S. M.; Bespalov, I.; Datler, M.; Vogel, D.; Budinska, Z.; Neyman, K. M.; Rupprechter, G. The Role of Metal/Oxide Interfaces for Long-Range Metal Particle Activation During CO Oxidation. *Nat. Mater.* **2018**, *17*, 519−522.

(5) Zhao, Z.-J.; Li, Z.; Cui, Y.; Zhu, H.; Schneider, W. F.; Delgass, W. N.; Ribeiro, F.; Greeley, J. Importance of Metal-Oxide Interfaces in Heterogeneous Catalysis: A Combined DFT, Microkinetic, and Experimental Study of Water-Gas Shift on Au/MgO. *J. Catal.* **2017**, *345*, 157−169.

(6) Ernst, F. Metal-Oxide Interfaces. *Mater. Sci. Eng. R Rep.* **1995**, *14*, 97−156.

(7) Campbell, C. T. Ultrathin Metal Films and Particles on Oxide Surfaces: Structural, Electronic and Chemisorptive Properties. *Surf. Sci. Rep.* **1997**, *27*, 1−111.

(8) Bäumer, M.; Freund, H.-J. Metal Deposits on Well-Ordered Oxide Films. *Prog. Surf. Sci.* **1999**, *61*, 127−198.

(9) Fu, Q.; Wagner, T. Interaction of Nanostructured Metal Overlayers with Oxide Surfaces. *Surf. Sci. Rep.* **2007**, *62*, 431−498.

(10) Hemmingson, S. L.; Campbell, C. T. Trends in Adhesion Energies of Metal Nanoparticles on Oxide Surfaces: Understanding Support Effects in Catalysis and Nanotechnology. *ACS Nano* **2017**, *11*, 1196−1203.

(11) Campbell, C. T.; Mao, Z. Chemical Potential of Metal Atoms in Supported Nanoparticles: Dependence upon Particle Size and Support. *ACS Catal.* **2017**, *7*, 8460−8466.

(12) Mao, Z.; Campbell, C. T. Predicting a Key Catalyst-Performance Descriptor for Supported Metal Nanoparticles: Metal Chemical Potential. *ACS Catal.* **2021**, *11*, 8284−8291.

(13) Campbell, C. T. Electronic Perturbations. *Nat. Chem.* **2012**, *4*, 597−598.

(14) Rice, P. S.; Hu, P. Understanding Supported Noble Metal Catalysts Using First-Principles Calculations. *J. Chem. Phys.* **2019**, *151*, 180902.

(15) Bruix, A.; Rodriguez, J. A.; Ramírez, P. J.; Senanayake, S. D.; Evans, J.; Park, J. B.; Stacchiola, D.; Liu, P.; Hrbek, J.; Illas, F. A New Type of Strong Metal-Support Interaction and the Production of H₂ through the Transformation of Water on Pt/CeO₂(111) and Pt/CeOₓ/TiO₂(110) Catalysts. *J. Am. Chem. Soc.* **2012**, *134*, 8968−8974.

(16) Vayssilov, G. N.; Lykhach, Y.; Migani, A.; Staudt, T.; Petrova, G. P.; Tsud, N.; Skála, T.; Bruix, A.; Illas, F.; Prince, K. C.; et al. Support Nanostructure Boosts Oxygen Transfer to Catalytically Active Platinum Nanoparticles. *Nat. Mater.* **2011**, *10*, 310−315.

(17) Lykhach, Y.; Faisal, F.; Skála, T.; Neitzel, A.; Tsud, N.; Vorokhta, M.; Dvořák, F.; Beranová, K.; Kosto, Y.; Prince, K. C.; et al. Interplay Between Metal-Support Interaction and Stability in Pt/Co₃O₄(111) Model Catalysts. *J. Mater. Chem. A* **2018**, *6*, 23078−23086.

(18) Lykhach, Y.; Kozlov, S. M.; Skála, T.; Tovt, A.; Stetsovych, V.; Tsud, N.; Dvořák, F.; Johánek, V.; Neitzel, A.; Mysliveček, J.; et al. Counting Electrons on Supported Nanoparticles. *Nat. Mater.* **2016**, *15*, 284−288.

(19) Tovt, A.; Bagolini, L.; Dvořák, F.; Tran, N.-D.; Vorokhta, M.; Beranová, K.; Johánek, V.; Farnesi Camellone, M.; Skála, T.; Matolínová, I.; et al. Ultimate Dispersion of Metallic and Ionic Platinum on Ceria. *J. Mater. Chem. A* **2019**, *7*, 13019−13028.

(20) Farnesi Camellone, M.; Dvořák, F.; Vorokhta, M.; Tovt, A.; Khalakhan, I.; Johánek, V.; Skála, T.; Matolínová, I.; Fabris, S.; Mysliveček, J. Adatom and Nanoparticle Dynamics on Single-Atom Catalyst Substrates. *ACS Catal.* **2022**, *12*, 4859−4871.

(21) Taleblou, M.; Camellone, M. F.; Fabris, S.; Piccinin, S. Oxidation of Gas-Phase and Supported Pt Nanoclusters: An Ab Initio Investigation. *J. Phys. Chem. C* **2022**, *126*, 10880−10888.

(22) Giannozzi, P.; Baroni, S.; Bonini, N.; Calandra, M.; Car, R.; Cavazzoni, C.; Ceresoli, D.; Chiarotti, G. L.; Dabo, M.; Dal Corso, I.; et al. QUANTUM ESPRESSO: A Modular and Open-Source Software Project for Quantum Simulations of Materials. *J. Phys.: Condens. Matter* **2009**, *21*, 395502.

(23) Giannozzi, P.; Andreussi, O.; Brumme, T.; Bunau, O.; Buongiorno Nardelli, M.; Calandra, M.; Car, R.; Cavazzoni, C.; Ceresoli, D.; Cococcioni, M.; Colonna, N.; et al. Advanced Capabilities for Materials Modelling with Quantum ESPRESSO. *J. Phys.: Condens. Matter* **2017**, *29*, 465901.

(24) Lykhach, Y.; Piccinin, S.; Skála, T.; Bertram, M.; Tsud, N.; Brummel, O.; Farnesi Camellone, M.; Beranová, K.; Neitzel, A.; Fabris, S.; et al. Quantitative Analysis of the Oxidation State of Cobalt Oxides by Resonant Photoemission Spectroscopy. *J. Phys. Chem. Lett.* **2019**, *10*, 6129−6136.

(25) Meyer, W.; Biedermann, K.; Gubo, M.; Hammer, L.; Heinz, K. Surface Structure of Polar Co₃O₄(111) Films Grown Epitaxially on Ir(100)-(1×1). *J. Phys.: Condens. Matter* **2008**, *20*, 265011.

(26) Biedermann, K.; Gubo, M.; Hammer, L.; Heinz, K. Phases and Phase Transitions of Hexagonal Cobalt Oxide Films on Ir(100)-(1 × 1). *J. Phys.: Condens. Matter* **2009**, *21*, 185003.

(27) Libra, J. *KolXPD: Spectroscopy Data Measurement and Processing.* http://www.kolibrik.net/science/kolxpd/ (accessed June 15, 2021).

(28) Stonkus, O. A.; Kardash, T. Y.; Slavinskaya, E. M.; Zaikovskii, V. I.; Boronin, A. I. Thermally Induced Structural Evolution of Palladium-Ceria Catalysts. Implication for CO Oxidation. *ChemCatChem* **2019**, *11*, 3505−3521.

(29) Bera, P.; Patil, K. C.; Jayaram, V.; Subbanna, G. N.; Hegde, M. S. Ionic Dispersion of Pt and Pd on CeO₂ by Combustion Method: Effect of Metal-Ceria Interaction on Catalytic Activities for NO Reduction and CO and Hydrocarbon Oxidation. *J. Catal.* **2000**, *196*, 293−301.

(30) Neitzel, A.; Figueroba, A.; Lykhach, Y.; Skála, T.; Vorokhta, M.; Tsud, N.; Mehl, S.; Ševčíková, K.; Prince, K. C.; Neyman, K. M.; et al. Atomically Dispersed Pd, Ni, and Pt Species in Ceria-Based Catalysts: Principal Differences in Stability and Reactivity. *J. Phys. Chem. C* **2016**, *120*, 9852−9862.

(31) Ketteler, G.; Ogletree, D. F.; Bluhm, H.; Liu, H.; Hebenstreit, E. L. D.; Salmeron, M. In Situ Spectroscopic Study of the Oxidation

and Reduction of Pd(111). *J. Am. Chem. Soc.* **2005**, *127*, 18269−18273.

(32) Kibis, L. S.; Titkov, A. I.; Stadnichenko, A. I.; Koscheev, S. V.; Boronin, A. I. X-Ray Photoelectron Spectroscopy Study of Pd Oxidation by RF Discharge in Oxygen. *Appl. Surf. Sci.* **2009**, *255*, 9248−9254.

(33) Schalow, T.; Laurin, M.; Brandt, B.; Schauermann, S.; Guimond, S.; Kuhlenbeck, H.; Starr, D. E.; Shaikhutdinov, S. K.; Libuda, J.; Freund, H.-J. Oxygen Storage at the Metal/Oxide Interface of Catalyst Nanoparticles. *Angew. Chem., Int. Ed.* **2005**, *44*, 7601−7605.

(34) Wang, H.; Gu, X.-K.; Zheng, X.; Pan, H.; Zhu, J.; Chen, S.; Cao, L.; Li, W.-X.; Lu, J. Disentangling the Size-Dependent Geometric and Electronic Effects of Palladium Nanocatalysts Beyond Selectivity. *Sci. Adv.* **2019**, *5*, No. eaat6413.

(35) Kaden, W. E.; Wu, T.; Kunkel, W. A.; Anderson, S. L. Electronic Structure Controls Reactivity of Size-Selected Pd Clusters Adsorbed on TiO_2 Surfaces. *Science* **2009**, *326*, 826−829.

(36) Martin, N. M.; Van den Bossche, M.; Grönbeck, H.; Hakanoglu, C.; Zhang, F.; Li, T.; Gustafson, J.; Weaver, J. F.; Lundgren, E. CO Adsorption on Clean and Oxidized Pd(111). *J. Phys. Chem. C* **2014**, *118*, 1118−1128.

(37) Surnev, S.; Sock, M.; Ramsey, M. G.; Netzer, F. P.; Wiklund, M.; Borg, M.; Andersen, J. N. CO Adsorption on Pd(111): A High-Resolution Core Level Photoemission and Electron Energy Loss Spectroscopy Study. *Surf. Sci.* **2000**, *470*, 171−185.

(38) Wertheim, G. K.; DiCenzo, S. B. Cluster Growth and Core-Electron Binding Energies in Supported Metal Clusters. *Phys. Rev. B Condens. Matter* **1988**, *37*, 844−847.

(39) Faisal, F.; Bertram, M.; Stumm, C.; Wähler, T.; Schuster, R.; Lykhach, Y.; Neitzel, A.; Skála, T.; Tsud, N.; Beranová, K.; et al. Electrocatalysis with Atomically Defined Model Systems: Metal-Support Interactions between Pt Nanoparticles and $Co_3O_4(111)$ under Ultrahigh Vacuum and in Liquid Electrolytes. *J. Phys. Chem. C* **2018**, *122*, 20787−20799.

(40) Bertram, M.; Prössl, C.; Ronovský, M.; Knöppel, J.; Matvija, P.; Fusek, L.; Skála, T.; Tsud, N.; Kastenmeier, M.; Matolín, V.; et al. Cobalt Oxide-Supported Pt Electrocatalysts: Intimate Correlation between Particle Size, Electronic Metal-Support Interaction and Stability. *J. Phys. Chem. Lett.* **2020**, *11*, 8365−8371.

(41) Bowker, M.; Davies, P. R. *Scanning Tunneling Microscopy in Surface Science*; Wiley: Weinheim, 2009.

(42) Kastenmeier, M.; Fusek, L.; Deng, X.; Skála, T.; Mehl, S.; Tsud, N.; Grau, S.; Stumm, C.; Uvarov, V.; Johánek, V.; et al. Particle Size and Shape Effects in Electrochemical Environments: Pd Particles Supported on Ordered $Co_3O_4(111)$ and Highly Oriented Pyrolytic Graphite. *J. Phys. Chem. C* **2022**, *126*, 12870−12881.

(43) Tanuma, S.; Powell, C. J.; Penn, D. R. Calculations of Electron Inelastic Mean Free Paths. V. Data for 14 Organic Compounds over the 50−2000 eV Range. *Surf. Interface Anal.* **1994**, *21*, 165−176.

(44) Bratsch, S. G. Standard Electrode Potentials and Temperature Coefficients in Water at 298.15 K. *J. Phys. Chem. Ref. Data* **1989**, *18*, 1−21.